October 15, 1999

Transparent stacked organic light emitting devices. I. Design principles and transparent compound electrodes

G. Gu
G. Parthasarathy
P. E. Burrows
Peifang Tian, *John Carroll University*
I. G. Hill, et al.

Transparent stacked organic light emitting devices. I. Design principles and transparent compound electrodes

G. Gu, G. Parthasarathy, P. E. Burrows, P. Tian, I. G. Hill, A. Kahn, and S. R. Forrest

Center for Photonics and Optoelectronic Materials, Department of Electrical Engineering
and Princeton Materials Institute, Princeton University, Princeton, New Jersey 08544

Vertical stacking of organic light emitting devices (OLEDs) that emit the three primary colors is a means for achieving full-color flat panel displays. The physics, performance, and applications of stacked OLEDs (SOLEDs) are discussed in this and the following paper (Papers I and II, respectively). In Paper I, we analyze optical microcavity effects that can distort the emission colors of SOLEDs if not properly controlled, and describe design principles to minimize these parasitic effects. We also describe the fabrication and operating characteristics of transparent contacts that are an integral part of SOLEDs. We demonstrate that both metal-containing and metal-free transparent electrodes can serve as efficient electron and hole injectors into the stacked organic semiconductor layers. Two different transparent SOLED structures (metal-containing and metal-free) that exhibit sufficient performance for many full-color display applications will be discussed in Paper II. © *1999 American Institute of Physics.* [S0021-8979(99)03120-5]

I. INTRODUCTION

Organic light emitting devices (OLEDs)[1] have shown sufficient brightness,[2,3] range of color,[2] and lifetime[4] for use in full-color, emissive flat panel displays.[3,5] To our knowledge, however, an acceptable technology for producing full-color OLED displays has not yet been reported. Among the several potential strategies[3] for making such full-color displays, one approach uses vertically stacked red (R), green (G), and blue (B) emitting OLEDs to form a pixel, leading to a threefold increase in resolution and display fill factor compared to the traditional side-by-side subpixel arrangement.[3,5]

Transparent OLEDs (TOLEDs)[6–8] are necessary components in the stacked OLED (SOLED) architecture since light emitted from a given subpixel must be transmitted through the adjacent subpixels in the stack to be viewed. A unique property of organic electroluminescent (EL) materials not shared by their inorganic counterparts is that the EL spectrum is substantially red shifted from the absorption band due to Franck–Condon molecular relaxation.[9] Hence, organic layers in OLEDs are often highly transparent over their own emission bands and throughout the visible spectrum. Previously, we demonstrated a TOLED with a composite transparent cathode composed of a very thin (~100 Å) metal film and a sputter-deposited indium tin oxide (ITO) cap.[6,7] A two-color SOLED was subsequently demonstrated by stacking a red-emitting OLED onto a blue-emitting TOLED, using the ITO cap of the bottom TOLED as the anode for the upper OLED.[10]

In the first three-color SOLED,[11] the thin semitransparent metal cathode of the bottom, blue-emitting subpixel also served as the cathode for the middle, green-emitting subpixel. This subpixel employed an inverted structure,[12] where the electron transport layer (ETL) was deposited onto the metal surface, followed by the deposition of the hole transport layer (HTL). The ITO anode of the middle subpixel was shared by the top subpixel capped by a thick metal cathode.

In these early SOLEDs,[10,11] the emission colors of some subpixels were substantially distorted by microcavity[13–15] resonances. Primary optical cavities were formed between reflective metal layers, while Fresnel reflection due to refractive index mismatch at every dielectric interface also contributed to the microcavity effects. We developed a quantitative model[16] of OLED microcavities, which was subsequently employed[17] to optimize the individual layer thicknesses and subpixel ordering to minimize these parasitic optical effects. Following the optimized design, we fabricated a full-color SOLED that had true R, G, and B color emission.[17]

Another problem of the early SOLEDs was the high operating voltage (20 V) resulting from poor carrier injection properties of the intermediate electrodes.[10,11,17] In particular, the metal cathode of an inverted OLED structure injects electrons inefficiently into the overlying ETL when compared to a metal cathode directly deposited onto the ETL surface.[12] On the other hand, the intermediate ITO anode layer deposited using the room temperature sputtering process developed to prevent damage to the underlying organic materials injects holes less efficiently into the overlying HTL than does a conventional, commercially obtained ITO film.[18] The ITO sputter process was therefore modified by introducing excess O_2 during the final stages of deposition, resulting in a dramatic decrease in the SOLED operating voltage.[18] Using this modified process, we demonstrated a high efficiency, low drive voltage, two color SOLED,[18] where two TOLEDs were used as subpixels to reduce internal reflections that lead to microcavity effects. A full color semitransparent SOLED will be described in article II.[19]

To further suppress microcavity effects and reduce optical absorption losses, very high transparency cathodes are desirable. Parthasarathy *et al.* demonstrated a metal-free cathode composed of a copper phthalocyanine (CuPc) thin film and an ITO overlayer which is >60% transparent

throughout the visible spectrum.[8] This cathode was incorporated into a SOLED, where three metal-free TOLEDs (MF-TOLEDs) are vertically stacked, giving satisfactory emission colors and operating voltages.[20]

In the three-color SOLEDs demonstrated thus far, adjacent subpixels share electrodes, preventing the separate referencing of the subpixel drive voltages to ground. The resulting need for a differential current drive scheme complicates the addressing circuitry, which may be undesirable in some cases.[3] To avoid this problem, insulating layers can be introduced to break the electrode connection between the subpixels. With the electrode between the two lower subpixels used as a common ground, the insertion of an insulating layer between the middle and top subpixels allows for a ground potential reference for each element in the stack. In addition, a highly transparent (~90%) metal-free contact using bathocuproine (BCP) instead of CuPc was employed, leading to a SOLED transparency of 70% across the visible spectral region. This optimized SOLED pixel will also be described in Paper II.[19]

In Paper I, we further discuss the optimization of SOLEDs. In particular, we discuss the suppression of color distorting microcavity effects, the reduction of operating voltage, and the improvement in contact transparency. In Paper II,[19] we will show that SOLEDs and metal-free SOLEDs (MF-SOLEDs) can have performance which in many cases exceeds that achieved using full-color OLED pixels arranged in a side-by-side configuration.

This article is organized as follows: Sec. II briefly describes a quantitative model of microcavity effects in OLEDs and then discusses the use of this model to minimize such effects. In Sec. III, we describe the fabrication and characteristics of metal-containing and metal-free transparent contacts, and discuss the oxygen enhanced ITO sputter deposition process needed to improve hole injection from such contacts. Finally, a brief summary is presented in Sec. VI.

In Paper II,[19] we will present a semitransparent, low operating voltage, full-color SOLED using metal-containing contacts, as well as a highly transparent MF-SOLED with a common ground reference to each subpixel in the stack. Addressing schemes for displays based on SOLEDs will be discussed, and the SOLED scheme will be compared with other strategies for achieving large full-color, OLED-based displays.

II. SOLED DESIGN BASED ON MICROCAVITY ANALYSIS

Organic light emitting devices generate light via radiative recombination of excitons on electrically excited molecules located in a layered structure. The OLED consists of reflective metallic electrodes and other partially reflecting interfaces between refractive index mismatched materials. These multiple layers act cooperatively to form an optical microcavity. The microcavity determines the electric field mode distribution, thereby modifying the exciton spontaneous emission transition rates, and hence the spectral distribution of EL intensity. In some applications, microcavity effects are desired to achieve directionality,[21] color saturation,[15,21] or lasing action.[22,23] In most OLEDs, how-
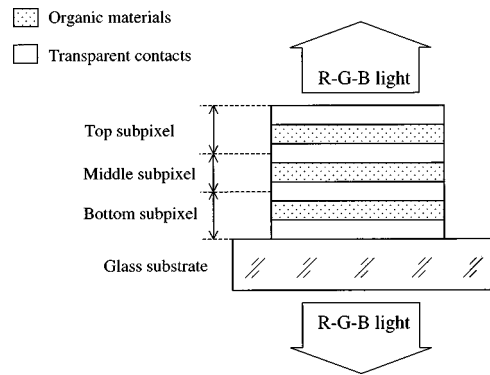

FIG. 1. Conceptual cross-section of a three-color SOLED. While transparent contacts are shared by adjacent subpixels, the top contact may be a thick, reflective metallic electrode in some cases.

ever, microcavity effects distort and cause an angular dependence of the emission colors. Figure 1 shows a conceptual cross-section of a three-color SOLED, where intermediate transparent contacts are shared by adjacent subpixels. The numerous layers form a complicated optical microcavity. Considering the ubiquity of microcavity effects in OLEDs and their impact on SOLED properties, they have been comprehensively modeled by our group.[16] Here, we use the model to optimize SOLED structures by choosing layer thicknesses and ordering that minimize the microcavity resonances.

A. Theory

The model deals with emission from an exciton placed in a one-dimensional (1D) layered structure. Each eigenmode is represented by a wave vector, $\mathbf{k}$, and its 1D electric field distribution along the direction normal to the material interfaces ($\hat{z}$) is found using Maxwell's equations with standard boundary conditions across the various layer interfaces. The radiation intensity emitted into an eigenmode of $\mathbf{k}$ by an exciton at position z is proportional to the transition rate given by Fermi's golden rule:

$$dW = 2\pi |\langle n|\mu \cdot \mathbf{E}(\mathbf{k},z)|m\rangle|^2 \delta(E_n - E_m - h\nu)/h, \quad (1)$$

where μ is the dipole moment, $\mathbf{E}(\mathbf{k},z)$ is the electric field for mode $\mathbf{k}$ at position z, E_n and E_m are eigenenergies of the initial ($|n\rangle$) and final ($|m\rangle$) exciton states, respectively, h is Planck's constant, and ν is the frequency of the emitted photon. For visible radiation, Eq. (1) is approximated by

$$dW = 2\pi |\langle n|\mu|m\rangle|^2 |\mathbf{E}(\mathbf{k},z)|^2 \delta(E_n - E_m - h\nu)/h, \quad (2)$$

since $\lambda \gg a$, the exciton radius. For an OLED, the glass substrate can be assumed to be infinitely thick, and hence propagation in this region is treated using ray optics. Having determined the electromagnetic field in the layered structure, we apply Eq. (2) to obtain the following expressions for the radiation rate of mode $\mathbf{k}$ into solid angle $d\Omega$ within the substrate:

$$dW_{TE} = W_0 \frac{1}{4\pi} \frac{n_G}{n_M} |E_Y(\mathbf{k},z)|^2 d\Omega \equiv W_0 f_{TE}(\lambda,\theta,z) d\Omega$$

$$(3)$$

for TE modes, and

$$dW_{TM} = W_0 \frac{1}{4\pi} \left[\frac{n_G^3}{n_M^5} \sin^2\theta |H_Y|^2 + \frac{n_G}{n_M^5 k_0^2} \left| \frac{dH_Y}{dz} \right|^2 \right] d\Omega$$

$$\equiv W_0 f_{TM}(\lambda,\theta,z) d\Omega \quad (4)$$

for TM modes, Here, W_0 is the intrinsic radiative transition rate of the excited molecule in vacuum, E_Y and H_Y are the in-plane components of the electric and magnetic fields normalized to the value at $z=\infty$, n_G is the refractive index of the glass substrate, n_M is the refractive index of the light emitting layer, θ is the angle between $\hat{z}$ and the propagation direction of mode **k** in the substrate, and $k_0 = 2\pi/\lambda$ is the free space wavevector for wavelength λ.

Equations (3) and (4) give the modification of the radiation rate into each mode for an EL source at position z. Assuming that the same number of excitons emit into TE and TM modes, we define

$$f(\lambda,\theta,z) \equiv [f_{TE}(\lambda,\theta,z) + f_{TM}(\lambda,\theta,z)]/2. \quad (5)$$

The emission spectrum of a beam at angle θ from $\hat{z}$ within the glass substrate can be expressed as

$$\Phi(\lambda,\theta) = \Phi_0(\lambda) F(\lambda,\theta). \quad (6)$$

Here, $\Phi_0(\lambda)$ is the intrinsic radiation spectrum of the emitting molecule which is approximated in calculations by the photoluminescence (PL) spectrum of the molecule measured from thick films or solutions, and the spectral modification factor, $F(\lambda,\theta)$, is the weighted sum of the spectral modifications $f(\lambda,\theta,z)$ of excitons across the emitting layer, viz.:

$$F(\lambda,\theta) = \int_{EL\ region} D(z) f(\lambda,\theta,z) dz. \quad (7)$$

Here, the exciton density, $D(z)$, is assumed to be an exponentially decaying function with a maximum at the interface where excitons are formed, and with a characteristic length equal to the exciton diffusion length, L_D (typically $\sim$200 Å for Alq$_3$).[9] The emission spectrum observed in a direction off-normal in air is obtained by using Snell's law and Eq. (6).

B. Optimizing SOLED structures to minimize microcavity effects

This model has been employed to determine the layer thicknesses and subpixel ordering in SOLEDs which minimize microcavity effects. While the first three-color SOLED exhibited severe color distortion due to microcavity effects,[11] analysis using the model described in Sec. II A shows that undistorted colors can be obtained with a similar structure by simply changing the ordering of the blue and green subpixels.[17] Stacked OLEDs have been fabricated using such optimized structures, which exhibit true R, G, and B emission colors over large viewing angles.[17,20]

Here, we analyze the microcavity effects in a previously demonstrated MF-SOLED[20] as an example to illustrate the use and predictive accuracy of the model. Figure 2 shows a schematic cross-section of that device, along with the composition, thickness, and function of each layer. The HTLs were composed of 4,4'-bis[N-(1-napthyl)-N-phenyl-

FIG. 2. Schematic cross-section of the example MF-SOLED used to illustrate the optimization of SOLED structures.

amino]biphenyl (α-NPD), while tris-(8-hydroxyquinoline) aluminum (Alq$_3$) films formed the green emitting and electron transport layers. The electron transporting emissive region of the blue subpixel consisted of a 350-Å-thick layer of bis-(8-hydroxy)quinaldine aluminum phenoxide (Alq'$_2$OPh) interposed between the HTL and the ETL, and that of the red subpixel consisted of 2, 3, 7, 8, 12, 13, 17, 18-octaethyl-21H,23H-porphine platinum (PtOEP),[24] doped at $\sim$9% (by mass) into Alq$_3$ by coevaporation. The metal-free transparent cathode of each subpixel consisted of a 55-Å-thick CuPc film and an ITO cap, which in the two lower subpixels also serves as an anode for an upper subpixel. Layers of CuPc were employed to improve the hole injection from these sputtered ITO anodes into overlying α-NPD HTLs, as will be discussed in Sec. III. We also analyze here, for comparison, a SOLED having a similar structure but with the CuPc thin films in the intermediate transparent contacts replaced by 100-Å-thick Mg:Ag films, and with the top metal-free contact replaced by a reflective, 1500-Å-thick Mg:Ag cathode. Refractive index dispersion was approximated for the organic and ITO layers using $n(\lambda) = n(\lambda_0) + a(\lambda-\lambda_0)^2$, where parameters λ_0, a, and $n(\lambda_0)$ are listed in Table I for each material. The complex refractive index data for CuPc and Mg are obtained from Refs. 26 and 27, respectively.

Figures 3(a) and 3(b) show the calculated spectral modification factors, $F(\lambda,0)$, for substrate normal emissions of the MF-SOLED and metal-containing, semitransparent SOLED, respectively. These curves show that the emission

TABLE I. Dispersion parameters of SOLED constituent materials used in microcavity modeling.[a]

Material[b]	λ_0 (μm)	$n(\lambda_0)$	a (μm^{-2})
Alq$_3$	0.60	1.72	1.8
α-NPD	0.60	1.78	4.5
Alq$_2$OPH	0.60	1.70	0
Sputtered ITO	0.83	1.95	1.95
Precoated ITO	0.60	1.80	9.0

[a]$n(\lambda) = n(\lambda_0) + n(\lambda-\lambda_0)$.
[b]Parameters for Alq$_3$ extracted from Ref. 25, and for all other materials measured in this work.
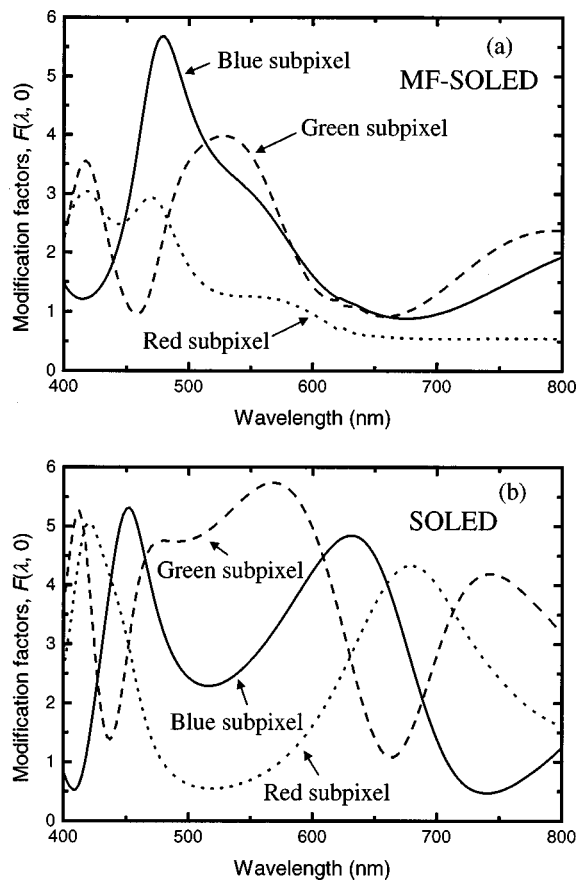
FIG. 3. Calculated spectral modification factors for substrate normal emission of (a) the example MF-SOLED shown in Fig. 2, and (b) a metal-containing SOLED with a similar structure.
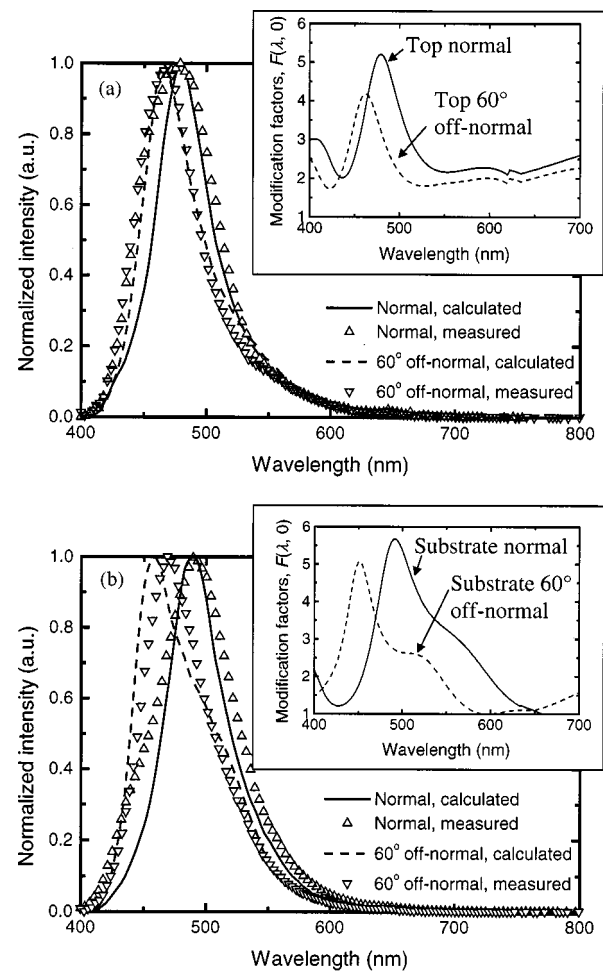

FIG. 4. Calculated (lines) and measured (symbols) top (a) and substrate (b) emission spectra of the middle (blue) subpixel of the example MF-SOLED in the normal and 60° off-normal directions. Insets: Calculated spectral modification factors in the normal (solid lines) and 60° off-normal directions (dashed lines) for the top (a) and substrate (b) emission of this subpixel.

of an MF-SOLED is less strongly affected by microcavity effects [i.e., wavelength variations in $F(\lambda,0)$ are smaller] compared to the metal containing SOLED due to the reduced internal reflections of the former device. The residual microcavity effects in the MF-SOLED, particularly at $\lambda < 500\,\text{nm}$, are primarily due to Fresnel reflections at the ITO/glass, ITO/CuPc, and ITO/air interfaces where refractive index mismatches are large. The resonance peaks [i.e., large $F(\lambda,0)$] in the blue spectral region exhibited by all subpixels in both structures are attributed to the cavities formed between contacts of the individual subpixels, since the $F(\lambda,0)$ of discrete OLEDs and MF-TOLEDs using similar layer thicknesses show similar peaks. These curves also show that red (top)/blue (middle)/green (bottom) is the optimal subpixel ordering for both SOLEDs: The metal-containing SOLED has a wide resonance peak in the red, while $F(\lambda,0)$ is flat in the red for the MF-SOLED. Both SOLED structures exhibit resonance peaks in the blue region, and each structure has a wide spectral window in the green.

The MF-SOLED is a transparent device emitting from both substrate and top surfaces. As an example, the insets of Figs. 4(a) and 4(b) show the spectral modification factors of the blue subpixel in the normal (solid lines) and 60° off-normal directions (dashed lines) for substrate and top viewing, respectively. The top emission for this particular choice of layer compositions and thicknesses is less strongly af-

fected by microcavity effects and has weaker angular dependence compared to that of the emission from the substrate. The calculated substrate and top emission spectra [Eq. (6)] are shown in Figs. 4(a) and 4(b), indicating a more saturated color and less angular dependence from top emission. The measured spectra of the MF-SOLED blue subpixel are also shown in Fig. 4, and are reasonably closely fit by the model. Similar results were found for the green and red subpixels. Hence, this particular device is more desirable for top viewing.

To optimize a SOLED structure, the spectral modification factors for all subpixel emissions are first calculated for the normal and off-normal viewing directions. Subpixel ordering is determined based on these preliminary results such that $F(\lambda,\theta)$ of each subpixel has a direction-insensitive spectral window, or flat region, overlapping its intrinsic emission spectrum, $\Phi_0(\lambda)$. Then, layer thicknesses are fine tuned to optimize the match between these windows and the intrinsic emission spectra. Emission spectra can then be calculated by multiplying the PL spectrum of the lumophore of each subpixel, $\Phi_0(\lambda)$, by the corresponding modification factor, $F(\lambda,\theta)$. If these spectra are not satisfactory in color

saturation or angular independence, new layer thicknesses or orderings are chosen and the process is iterated. In the case of transparent SOLEDs, the structures optimized for bottom and top viewing usually differ.

III. TRANSPARENT COMPOUND CONTACTS

As shown in Fig. 1, in most cases each transparent contact in a SOLED injects carriers of different polarities into the adjacent upper and lower stacked elements. The injection properties and transparencies of the contacts influence the operating voltages and efficiencies of all the light emitters in the stack. Furthermore, the residual reflection of the contacts is responsible for the formation of optical microcavities as discussed in Sec. II. Hence, highly transparent contacts with appropriate carrier injection properties are required in practical SOLEDs. In this section we discuss methods to achieve transparent compound contacts that efficiently inject both electrons and holes into organic thin films.

A. Transparent cathodes using thin metal films

For semitransparent SOLEDs, each subpixel contains a compound ITO/Mg:Ag cathode, whose ITO layer may be shared as the anode by an upper subpixel. To examine the properties of this electrode, we fabricated a discrete TOLED as follows: A commercially obtained ITO thin film precoated on a glass substrate[28] was cleaned[9] and treated for 2 min in a 31 W rf oxygen plasma, followed by sequential thermal evaporation in a vacuum of $<10^{-6}$ Torr of a 500-Å-thick HTL of α-NPD, and an ETL composed of a 350-Å-thick emissive region of Alq_3 doped at 0.8% (by mass) with N,N-dimethyl quinacridone (DMQA) capped with a 150-Å-thick Alq_3 film. After the deposition of a ~100-Å-thick Mg:Ag (9:1 by mass) film, the sample was transferred without exposure to atmosphere into a sputter deposition chamber through a glove box filled with N_2 where the moisture level was <2 ppm. A 500-Å-thick ITO cap was then sputtered from a 3-in.-diam target using 130 W rf power, corresponding to a deposition rate of 67 Å/min. The target was composed of 10% SnO_2 and 90% In_2O_3 by mass with 99% purity, and was housed in a magnetron sputtering gun facing the sample at a 45° tilt angle. Both the sample holder and the target were water cooled. The pressure during the sputter process was 2 mTorr, with the Ar flow controlled at 140 sccm.

Figure 5 shows the current density vs voltage $(J-V)$ characteristics of a typical TOLED, along with those of a conventional OLED using a thick Mg:Ag cathode. The $J-V$ characteristics of the two devices whose organic layers were grown simultaneously are not significantly different. The power law dependence of J or V at $V>4$ V indicates trap-limited conduction characteristic of small molecule OLEDs.[9] At $J=10$ mA/cm^2 (where the device luminance is typically >100 cd/m^2), the operating voltage of the TOLED is (5.5 ± 0.1) V, compared to (5.1 ± 0.1) V for the conventional OLED. The small increase in operating voltage for the TOLED may be due to the additional resistance at the Mg:Ag/ITO interface resulting from the barrier formed by the oxidation of Mg:Ag during ITO deposition, which may also be responsible for the adhesion of the ITO overlayer.[6] The substrate emission quantum efficiency of such TOLEDs
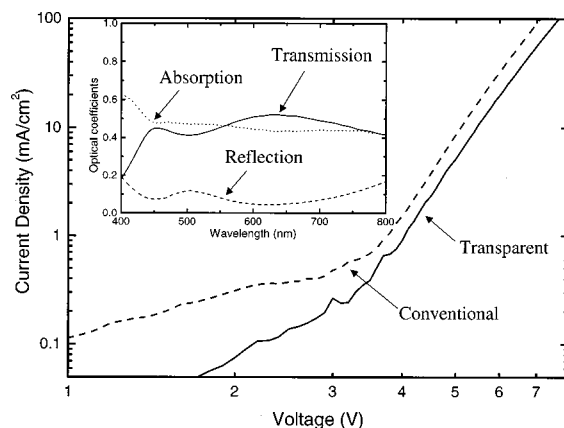
FIG. 5. Current density vs voltage characteristics of a transparent and a conventional OLED made under similar conditions. Inset: Optical transmission, reflection, and absorption spectra of the TOLED.

is $(0.35 \pm 0.02)\%$, and the bottom-to-top emission optical power ratio is 1:0.57. Hence, the total external quantum efficiency of the TOLED is $(0.55 \pm 0.03)\%$, which is ~75% that of the conventional OLED of $(0.79 \pm 0.05)\%$. We attribute this difference to optical absorption of the semitransparent cathode, and to exciton quenching near the cathode where damage is incurred during sputtering. The quenching effect is somewhat reduced by growing a thin (150 Å) Alq_3 buffer layer between the Mg:Ag and the Alq_3:DMQA luminescent layer.

The inset of Fig. 5 shows the optical transmission, reflection, and absorption of the TOLEDs. The device transparency is between 40% and 52% across the visible spectrum. This is somewhat lower than the 60% to 70% transparency achieved previously,[6] possibly due to the use of a slightly thicker Mg:Ag film and a less transparent ITO overlayer. Since the Mg:Ag layer absorption increases exponentially with thickness, a small deviation in thickness results in a considerable change in transparency. The thinnest Mg:Ag layer used thus far in a working TOLED is 60 Å, corresponding to a contact transparency of 81% and a total device transparency of 71%.[6] Hence, tight control of the Mg:Ag thickness is required to achieve operational devices with high transparency. Previously,[6] a small concentration of O_2 was introduced into the sputtering chamber during the ITO overlayer deposition to prevent the formation of a light absorbing Sn_3O_4-like phase in Sn-rich regions.[29] Excess O_2 in the sputtering gas, however, decreases oxygen vacancies in the film, thereby decreasing its electrical conductivity. For a given deposition rate determined by the sputtering power density, therefore, there is an optimal O_2 concentration range leading to both satisfactory transparency and conductivity. While a dramatic increase in the ITO sheet resistance was observed on adding O_2 during film growth using this sputterer, the expected concomitant increase in transparency did not occur.[30] The geometric difference between this sputtering process and that used previously[6] may be responsible for such a discrepancy in the dependence of transparency on the O_2 a concentration. The optimal sputterer configuration and
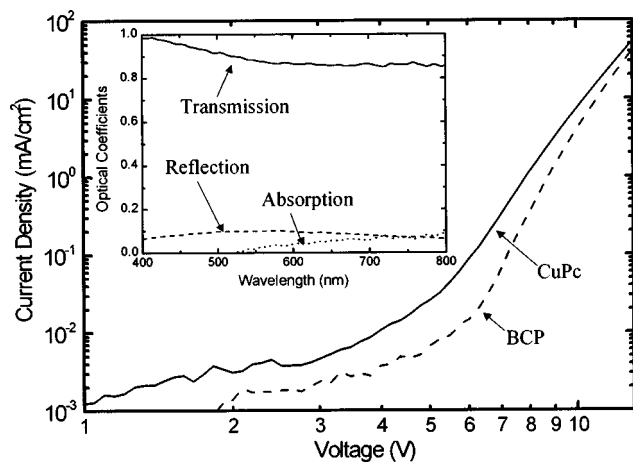
FIG. 6. Current density vs voltage characteristics of MF-TOLEDs using BCP (dashed line) and CuPc (solid line) in the transparent contacts. Inset: Optical transmission, reflection, and absorption spectra of the MF-TOLED using BCP in the metal-free contact.
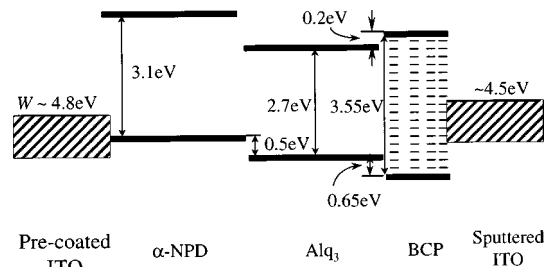

FIG. 7. Energy diagram of the MF-TOLED using a BCP EIL. The HOMO-HOMO offset energies and optical energy gaps are measured in this work or taken from Refs. 31 and 32. The work functions (*W*) of the oxygen plasma treated precoated, and the room-temperature sputtered ITO are estimated according to their hole injection properties.

O_2 concentration for achieving both satisfactory ITO film conductance and transparency remain to be found.

B. Metal-free transparent cathodes

When used in a SOLED, the Mg:Ag/ITO transparent contact has sufficient residual absorption to reduce the external efficiencies of the stacked emitters,[3,5] and sufficient reflection to cause microcavity effects that distort the emission colors.[11] Furthermore, the Mg:Ag film thickness must be tightly controlled to achieve operational devices with high transparency. On the other hand, metal-free TOLEDs have been demonstrated to minimize contact absorption and reflection.[8] To optimize these devices for use in SOLEDs, discrete MF-TOLEDs were fabricated as follows: After cleaning and oxygen plasma treatment of two ITO precoated glass substrates,[28] a 450-Å-thick α-NPD HTL was thermally deposited, followed by a 500-Å-thick Alq_3 ETL. Then, a 50-Å-thick bathocuproine (BCP) film was deposited onto one of the samples and a 50-Å-thick CuPc film onto the other. The samples were transferred with minimal air exposure to a sputtering chamber, where a 500-Å-thick ITO overlayer was sputtered at 5 W from a 2-in.-diam target. The sputtering gas pressure was 5 mTorr, with Ar and O_2 flows regulated at 200 and 0.1 sccm, respectively. Here, the optimal O_2 concentration for achieving both satisfactory film conductivity and transparency ranges from 0% to 0.05% for a sputtering power of 5 W, resulting in a $\sim$300 $\Omega/\square$ sheet resistance for a 500-Å-thick film. The BCP or CuPc film in the compound cathode serves as an electron injection layer (EIL), as well as a protection layer preventing damage during subsequent ITO sputter deposition.

The inset of Fig. 6 shows the optical transmission, reflection, and absorption of the MF-TOLED using BCP as the EIL. This device is $\sim$90% transparent throughout the visible region with losses primarily due to reflection. This represents a significant improvement relative to the metal-containing TOLEDs. The use of the highly transparent BCP layer in the transparent contact also reduces contact absorption relative

to the contacts using CuPc.[8] The transmission and absorption spectra of an MF-TOLED using one CuPc buffer layer in the compound cathode and another as a hole injection layer have been published elsewhere.[8] While exhibiting a maximum transmission of 84% at $\lambda = 550$ nm, this latter device is only 65% transparent at $\lambda = 620$ and 665 nm, due to the strong CuPc *Q*-band absorption peaks.[8] When used in SOLEDs, the CuPc layers in the multiple contacts can lead to considerable absorption, reducing the external efficiencies of the red-emitting subpixels. Hence, metal-free contacts based on highly transparent materials such as BCP are desirable to reduce these collective absorption losses.

Figure 6 shows the J–V characteristics of the two MF-TOLEDs. At $J = 10$ mA/cm^2, the operating voltage is (10.4 $\pm$ 0.3) V for the device using CuPc, compared to a voltage of (5.9 $\pm$ 0.8) V for a conventional OLED using similar HTL and ETL compositions and thicknesses (cf. Fig. 5). The operating voltage required to achieve the same current density for the MF-TOLED using BCP is (11.0 $\pm$ 0.3) V. Relative to the TOLED using the Mg:Ag/ITO cathode, the use of metal-free cathodes results in a significant increase in device transparency, but also leads to a $\sim$5 V increase in operating voltage (at $J = 10$ mA/cm^2). The total external quantum efficiencies are (0.35 $\pm$ 0.02)% and (0.28 $\pm$ 0.02)% for the devices using BCP and CuPc, respectively. Hence, the device using BCP requires a slightly higher operating voltage, but exhibits higher efficiency due to the lack of an absorptive EIL.

The electron injection from the metal-free cathode has been attributed to a high density of midgap states in the protective EIL induced by the high-energy particle bombardment during the ITO sputtering process.[8] Figure 7 shows the energy diagram of the MF-TOLED using a BCP EIL. The energy diagram is constructed using the (HOMO)-highest occupied molecular orbital-HOMO offsets measured by photoemission spectroscopy.[31,32] The energy difference between the HOMO and (LUMO) lowest unoccupied molecular orbital, corresponds to the optical band gap for each material. We estimate the work function, *W*, of the ITO overlayer sputtered without excess O_2 to be $\sim$4.5 V, consistent with its poor hole injection properties (cf. Sec. III C and Refs. 33 and 34). While there is a large barrier ($\sim$1.2 eV) to electron injection at the ITO/BCP interface, the midgap states induced during the energetic sputtering process result in effi-

cient electron injection from the ITO overlayer to the ETL. These states, whose density decreases away from the ITO interface, provide small energy ''steps'' which can be easily surmounted by injected electrons. The residual energy barrier, along with the difficulty of electron conduction through the midgap states, may account for the relatively high operating voltage and reduced efficiency of the MF-TOLEDs. The precoated ITO anode has a high work function ($\sim$4.8 eV) as a result of oxygen plasma treatment,[34,35] leading to efficient hole injection at the ITO/α-NPD interface (cf. Sec. III C).

The BCP or CuPc EIL also serves as a protection layer. Evidence for surface damage was obtained by reducing the EIL thickness to 30 Å, which resulted in a reduction in the yield of operating MF-TOLEDs.[8] The limited sputter damage to the EIL is attributed to the extended conjugated electron orbitals in the large planar molecules which efficiently distribute the impact energy of the sputtered atoms over the numerous molecular bonds.[8]

To accelerate the MF-TOLED fabrication, the ITO cap was sputtered at 50 W rf power from a 3-in.-diam target, resulting in a deposition rate of 30 Å/min. The operating voltage required at $J=10\,\mathrm{mA/cm^2}$ was 15 V, and the total external quantum efficiency was 0.42%. The increase in operating voltage relative to the MF-TOLEDs using low-power sputtered ITO caps is possibly due to the thicker (100 Å) BCP layer and residual damage to the ETL. Methods to achieve a faster fabrication process for MF-TOLEDs without degrading device performance remain to be explored.

C. Transparent contacts with improved hole injection

While the transparent cathode injects electrons into the ETL of a TOLED, in a SOLED the ITO cap layer also serves as the anode of the subpixel deposited onto its surface. Although the transparent contacts form reasonably good cathodes, early SOLEDs[10,11,17] exhibited very high operating voltage (20 V) and/or low quantum efficiencies for the upper subpixels due to inefficient hole injection from the room-temperature sputtered ITO layer into the overlying HTL. To improve its hole injection properties, excess O_2 was introduced into the chamber during the final stages of ITO deposition. The bulk ITO film is sputtered using a mixture of Ar and O_2, with the O_2 concentration optimized for the deposition rate determined by the rf power to achieve a satisfactory combination of conductivity and transparency. For deposition of the last 60–100 Å, the O_2 concentration is increased. Since excess O_2 increases the resistivity of the sputtered ITO film, it was only used during the final stages of deposition, resulting in a sheet resistance of 300–500 $\Omega/\square$ for a 400-Å-thick film, not significantly different from that achieved without introducing excess O_2.

To study the effect of excess O_2 in the sputtering gas, ITO thin films were sputter deposited onto precleaned glass microscope slides held at room temperature at 5 W rf power from a 2-in.-diam target. A 150 sccm Ar flow was used throughout the deposition of the 400-Å-thick films. Three different film deposition conditions were studied: (A) No O_2 was used. (B) Oxygen was introduced for deposition of the
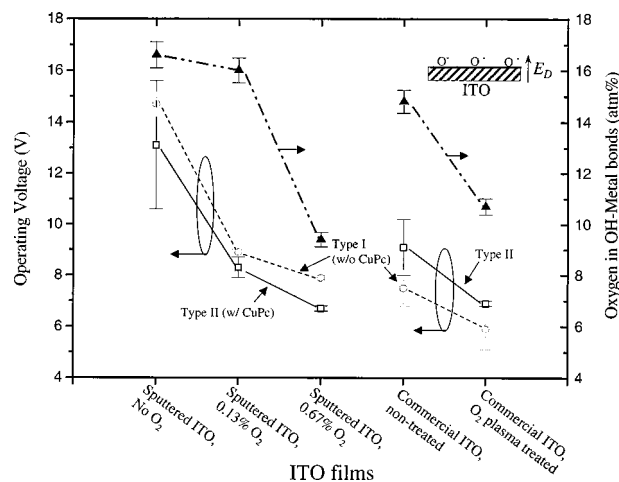

FIG. 8. Operating voltages at a current density $J=10\,\mathrm{mA/cm^2}$ for OLEDs deposited on various ITO thin films. Also shown are atomic concentrations of oxygen atoms in OH-metal bonds. Inset: Schematic illustration of the hole injection enhancing dipoles resulting from the surface oxygen radicals.

last 80 Å, first at a concentration of 0.067%, and subsequently increased to 0.13% for the final 20 Å, (C) Oxygen was introduced for deposition of the last 80 Å, first at a concentration of 0.13% and then increased to 0.67% for the final 20Å. Two types of OLEDs were fabricated on each of the ITO films, as well as on two commercially obtained,[28] precoated ITO films, one of which was treated for 2 min in a 31 W rf oxygen plasma. Each ''type I'' OLED consisted of a 400-Å-thick HTL of α-NPD, a 500-Å-thick ETL of Alq$_3$, and a 1500 Å cathode of Mg:Ag (9:1 by mass) capped with a 500-Å-thick Ag film. ''Type II'' OLEDs used an identical HTL/ETL/cathode structure but with a 50-Å-thick hole injection layer (HIL) of CuPc inserted between the HTL and the ITO anode.

Figure 8 shows the OLED operating voltages at $J=10\,\mathrm{mA/cm^2}$, where the error bars represent spreads in the data for a sample of 10 devices. The room-temperature sputter-deposited ITO films are labeled by the O_2 concentration used for the deposition of the final 20 Å. Oxygen plasma treatment leads to a small but significant improvement in hole injection from the commercial ITO, consistent with previous reports.[35,36] For room-temperature sputtered films, a small amount of oxygen introduced during the final stage of deposition leads to a dramatic improvement in hole injection, manifested by a 6–8 V decrease in OLED operating voltage. While lower operating voltages were achieved without CuPc layers for OLEDs on commercial ITO films, CuPc improves hole injection from the room-temperature sputtered ITO into HTLs, resulting in a $\sim$1 V reduction in the operating voltage for type II compared to type I structures. Hence, the modified ITO sputter process using excess O_2 during the final stages of deposition, along with a 50-Å-thick hole injection layer of CuPc, significantly improves the operating voltage of OLEDs deposited onto room-temperature sputtered ITO films. The external quantum efficiencies of these OLEDs are all $(0.7\pm0.1)\%$.

Figure 9 shows the forward and reverse biased $J-V$ characteristics of two identical OLEDs using CuPc hole injection layers, one fabricated on an ITO film sputter depos-
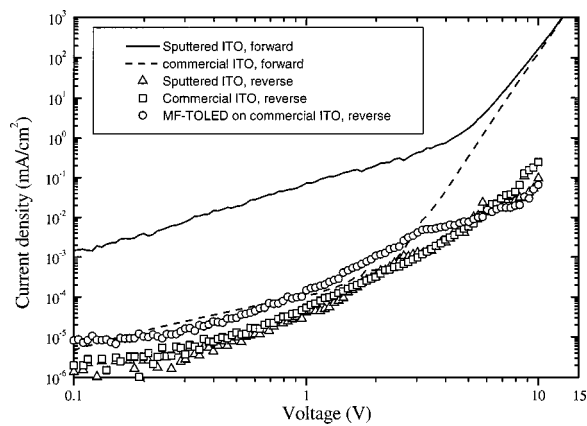
FIG. 9. Forward- and reverse-biased current density vs voltage ($J-V$) characteristics of identical OLEDs fabricated on an ITO film sputtered using 0.67% O_2 during the deposition of the final 20 Å [process (C)], and an oxygen plasma treated, commercially precoated ITO film. Reverse current density and voltage are taken as positive values. Also shown for comparison is the reverse biased $J-V$ curve of an MF-TOLED using identical organic layer thicknesses grown on commercial ITO.
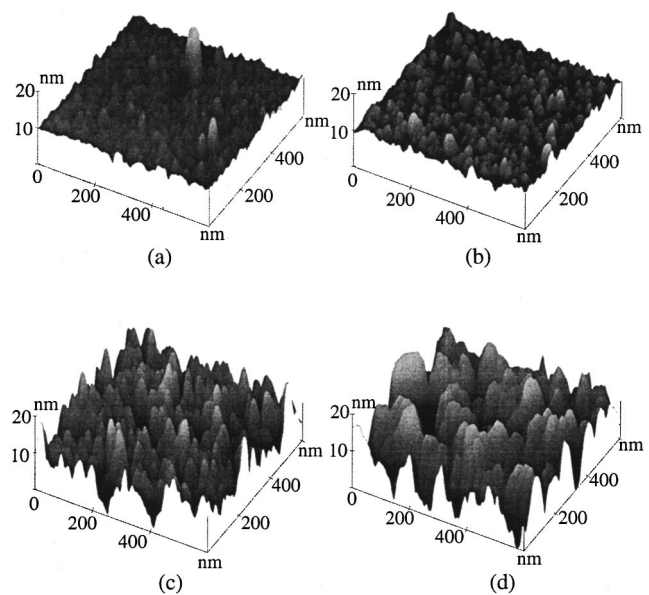

FIG. 10. AFM images of (a) an ITO film sputtered on a room-temperature substrate without using O_2 in the sputtering gas [process (A)], (b) an ITO film sputtered on a room-temperature substrate using 0.67% O_2 during the deposition of the final 20 Å [process (C)], (c) a nontreated commercial ITO film, and (d) a oxygen plasma treated commercial ITO film.

ited using process (C), and the other on an oxygen plasma treated, commercially precoated ITO film. While the operating voltages required to achieve a given current density are comparable for the two devices at high forward bias, the low voltage leakage current is significantly higher for the device using room-temperature sputtered ITO. Interestingly, the reverse biased leakage current, which should be low to enable passive matrix addressing, is comparable for both devices. To check if the use of a metal-free contact affects the reverse biased current, Fig. 9 also shows the reverse-biased $J-V$ characteristics of a typical MF-TOLED using identical organic layer thicknesses grown on commercial ITO. This device exhibits only a slightly higher reverse current than that of conventional OLEDs.

In an attempt to understand the reason for the differences in hole injection properties of the various ITO films, we examined their surface stoichiometry using x-ray photoelectron spectroscopy (XPS). The five films in Fig. 8 were examined at a 20° electron exit angle, corresponding to a probe depth of 20 Å. The surface species detected include Sn^{4+}, In^{3+}, OH^-, metal oxides, C–C, C–O, and COO^-. For both room-temperature sputtered and commercially precoated ITO films, we observe a strong correlation between the concentration of hydroxyl groups on an ITO film surface and OLED operating voltage.

The negative correlation between the surface OH group concentration and the hole injection properties of ITO films can be attributed to the formation of a dipole layer at the film surface. A possible source of the dipole is the formation of oxygen radicals during oxygen plasma treatment of ITO, or during the rf sputtering of ITO with excess oxygen[37] (see inset, Fig. 8). The electronegative oxygen radicals replace the OH groups and induce a surface dipole layer that increases ITO work function and decreases the barrier to hole injection at the ITO/organic material interface. Note that residual OH left on the surface in the absence of these oxygen treatments results in an oppositely directed dipole field

which can further impede injection as compared to the unhyroxylated surface.

We also observe considerable differences between the In/Sn atomic ratio of the ITO films sputtered using excess O_2 [In/Sn$=10.9\pm0.5$ and 10.8 ± 0.5 for processes (B) and (C), respectively] and no O_2 [In/Sn$=7.2\pm0.4$ for process (A)], while the In/Sn ratio of the plasma treated and nontreated commercial ITO films are identical within the measurement resolution (In/Sn$=7.7\pm0.4$ for both). The higher In/Sn ratio of ITO films sputtered using excess O_2 might also increase the work function, since Sn doping is *n* type in ITO.[29] The increase in work function due to both of the existence of the dipole layer and the higher In/Sn ratio are consistent with the observed improvement in hole injection.

In the SOLED structure, it is imperative that the sputtered ITO film be smooth to avoid shorting in the subpixel deposited onto its surface. Hence, we examined the surface morphology of the various ITO films using atomic force microcopy (AFM). Representative AFM images of sputter-deposited and commercially precoated ITO films are shown in Fig. 10. Table II lists the typical grain size, root–mean–square (rms) roughness, and mean roughness of the various films studied. We observe that the room-temperature sputtered ITO films have smoother surfaces (8.1–11 nm rms roughness) as compared with commercial films (34 nm rms roughness). While the grain sizes of the untreated commercial and the room-temperature sputtered films are comparable, the oxygen plasma treatment of the commercial film leads to a dramatic increase in the grain size, which may be related to improvements in hole injection. There is no appreciable difference in surface morphology between the various room-temperature sputtered ITO films using different O_2 concentrations.

TABLE II. Typical grain size and mean roughness of ITO films measured by AFM.

ITO films	Typical grain size (nm)	rms roughness (Å)	Mean roughness (Å)
Commercial, nontreated	20–60	34	26
Commercial, oxygen plasma treated	~100	46	36
Room-temperature sputtered, no O_2	20–60	11	6.5
Room-temperature sputtered, 0.2 sccm O_2	20–60	8.6	6.4
Room-temperature sputtered, 1.0 sccm O_2	20–60	8.1	6.3

In summary, efficient hole injection from room-temperature sputtered ITO thin films into an overlying organic layer has been achieved by introducing excess O_2 into the sputtering gas during the final stages of deposition. With the assistance of a CuPc hole injection layer, operating voltages comparable to those of OLEDs using oxygen plasma treated, commercial ITO anodes were achieved. Correlations were observed between device operating voltage and ITO surface stoichiometry. The surface morphologies of the sputtered ITO films are quite smooth, providing reliable contacts for SOLED subpixels deposited onto their surfaces.

IV. SUMMARY

In this article, we addressed the principles of structure design and transparent compound contacts. Optical micro-cavity effects, which distort emission colors if not properly controlled, have been thoroughly studied and quantitatively modeled. The analysis shows that microcavity effects can be suppressed by replacing reflective, metal-containing contacts with highly transparent, metal-free contacts. Furthermore, the model is employed to determine constituent layer thicknesses and subpixel ordering that minimize these effects. The fabrication of both metal-containing and metal-free transparent compound electrodes were discussed. The fabrication of metal-containing transparent cathodes has been dramatically expedited by increasing the rf sputtering power to >130 W. These contacts exhibit efficient electron injection comparable to conventional metal cathodes. Very high transparency, metal-free contacts have also been demonstrated with reasonably good electron injection properties. Efficient hole injection from the room-temperature sputtered ITO into organic thin films has been achieved. Based on the design principles and transparent contacts presented here, we will describe high performance metal-containing and metal-free SOLEDs in Paper II.[19]

ACKNOWLEDGMENTS

[1] C. W. Tang and S. A. VanSlyke, Appl. Phys. Lett. **51**, 913 (1987).
[2] C. W. Tang, Society for Information Display, International Symposium Digest of Technical Papers, Vol. 27, 181 (1996).
[3] G. Gu and S. R. Forrest, IEEE J. Sel. Top. Quantum Electron. **4**, 83 (1998).
[4] S. A. VanSlyke, C. H. Chen, and C. W. Tang, Appl. Phys. Lett. **69**, 2160 (1996).
[5] P. E. Burrows, G. Gu, V. Bulović, S. R. Forrest, and M. E. Thompson, IEEE Trans. Electron Devices **44**, 1188 (1997).
[6] G. Gu, V. Bulovic, P. E. Burrows, S. R. Forrest, and M. E. Thompson, Appl. Phys. Lett. **68**, 2606 (1996).
[7] V. Bulovic, G. Gu, P. E. Burrows, S. R. Forrest, and M. E. Thompson, Nature (London) **380**, 29 (1996).
[8] G. Parthasarathy, P. E. Burrows, V. Khalfin, V. G. Kozlov, and S. R. Forrest, Appl. Phys. Lett. **72**, 2138 (1998).
[9] P. E. Burrows, Z. Shen, V. Bulovic, D. M. McCarty, S. R. Forrest, J. A. Cronin, and M. E. Thompson, J. Appl. Phys. **79**, 7991 (1996).
[10] P. E. Burrows, S. R. Forrest, S. P. Sibley, and M. E. Thompson, Appl. Phys. Lett. **69**, 2959 (1996).
[11] Z. Shen, P. E. Burrows, V. Bulovic, S. R. Forrest, and M. E. Thompson, Science **276**, 2009 (1997).
[12] V. Bulovic, P. Tian, P. E. Burrows, M. R. Gokhale, S. R. Forrest, and M. E. Thompson, Appl. Phys. Lett. **70**, 2954 (1997).
[13] T. Nakayama, Y. Itoh, and A. Kakuta, Appl. Phys. Lett. **63**, 594 (1993).
[14] N. Takada, T. Tsutsui, and S. Saito, Appl. Phys. Lett. **63**, 2032 (1993).
[15] A. Dodabalapur, L. J. Rothberg, T. M. Miller, and E. W. Kwock, Appl. Phys. Lett. **64**, 2486 (1994).
[16] V. Bulovic, V. Khalfin, G. Gu, P. E. Burrows, and S. R. Forrest, Phys. Rev. B **58**, 3730 (1998).
[17] P. E. Burrows, V. Khalfin, G. Gu, and S. R. Forrest, Appl. Phys. Lett. **73**, 142 (1998).
[18] G. Gu, V. Khalfin, and S. R. Forrest, Appl. Phys. Lett. **73**, 2399 (1998).
[19] G. Gu, G. Parthasarathy, P. Tian, P. E. Burrows, and S. R. Forrest, J. Appl. Phys. **86**, 4076 (1999), following paper.
[20] G. Gu, G. Parthasarathy, and S. R. Forrest, Appl. Phys. Lett. **73**, 2399 (1998).
[21] O. Yokoyama, S. Miyashita, T. Shimoda, S. Tokito, K. Noda, Y. Taga, 9th Intern'l Workshop on Inorg. and Org. EL, Sept. 1998, Bend, OR (unpublished), p. 159.
[22] V. G. Kozlov, V. Bulovic, P. E. Burrows, and S. R. Forrest, Nature (London) **389**, 362 (1997).
[23] V. G. Kozlov, V. Bulovic, P. E. Burrows, M. Baldo, V. B. Khalfin, G. Parthasarathy, S. R. Forrest, Y. You, and M. E. Thompson, J. Appl. Phys. **84**, 4096 (1998).
[24] M. Baldo, D. F. O'Brien, Y. You, A. Shoustikov, S. Sibley, M. E. Thompson, and S. R. Forrest, Nature (London) **395**, 151 (1998).
[25] F. G. Celii, T. B. Harton, and O. F. Phillips, J. Electron. Mater. **26**, 366 (1997).
[26] B. H. Schechtman and W. E. Spicer, J. Mol. Spectrosc. **33**, 28 (1970).
[27] D. R. Lide, *CRC Handbook of Chemistry and Physics*, 79th ed. (Chemical Rubber, Boca Raton, FL, 1998), pp. 12–134.
[28] Donnelly Applied Films Corp., 6797-T Winchester Circle, Boulder, CO 80301.
[29] J. C. C. Fan and J. B. Goodenough, J. Appl. Phys. **48**, 3524 (1977).
[30] P. E. Burrows, G. Gu, E. P. Vicenzi, and S. R. Forrest (unpublished).
[31] I. G. Hill and A. Kahn, Proceedings of the SPIE Conference on Organic Light-Emitting Materials and Devices II, San Diego, CA, Vol. 3476, 1998, p. 168.
[32] I. G. Hill and A. Kahn (unpublished).
[33] Th. Kugler, Å. Johansson, I. Dalsegg, U. Gelius, and W. R. Salaneck, Synth. Met. **91**, 143 (1997).
[34] J. S. Kim, M. Granström, R. H. Friend, N. Johansson, W. R. Salaneck, R. Daik, W. J. Feast, and F. Cacialli, J. Appl. Phys. **84**, 6859 (1998).
[35] C. C. Wu, C. I. Wu, J. C. Sturm, and Kahn, Appl. Phys. Lett. **70**, 1348 (1997).
[36] S. Fujita, T. Sakamoto, K. Ueda, K. Ohta, and S. Fujita, Jpn. J. Appl. Phys., Part 1 **36**, 350 (1997).
[37] D. Markiewicz, J. Schwartz, I. G. Hill, and A. Kahn (unpublished).